Article type: Research Paper

Title Catalyst nanoparticle growth dynamics and their influence on product morphology in a CVD process for continuous carbon nanotube synthesis

Author(s), and Corresponding Author(s): Christian Hoecker[a], Fiona Smail[b], Mark Bajada[a], Martin Pick[b], Adam Boies[a,*]

[a] University of Cambridge, Department of Engineering, Cambridge CB2 1PZ, United Kingdom

[b] Q-Flo Limited, BioCity, Pennyfoot Street, Nottingham NG1 1GF, United Kingdom

Abstract

Extrapolating the properties of individual CNTs into macro-scale CNT materials using a continuous and cost effective process offers enormous potential for a variety of applications. The floating catalyst chemical vapor deposition (FCCVD) method discussed in this paper bridges the gap between generating nano- and macro-scale CNT material and has already been adopted by industry for exploitation. A deep understanding of the phenomena occurring within the FCCVD reactor is thereby key to producing the desired CNT product and successfully scaling up the process further. This paper correlates information on decomposition of reactants, axial catalyst nanoparticle dynamics and the morphology of the resultant CNTs and shows how these are strongly related to the temperature and chemical availability within the reactor. For the first time, in-situ measurements of catalyst particle size distributions coupled with reactant decomposition profiles and a detailed axial SEM study of formed CNT materials reveal specific domains that have important implications for scale-up. A novel observation is the formation, disappearance and reformation of catalyst nanoparticles along the reactor axis, caused by their evaporation and re-condensation and mapping of different CNT morphologies as a result of this process.

1. Introduction

Individual CNTs have exceptional mechanical, thermal and electrical properties, with tensile strengths up to 100 GPa, thermal conductivities up to 3000 W m^{-1} K^{-1} and electrical resistivities as low as 5×10^{-6} Ω cm [1–3]. However, the ability to translate the superior properties of individual CNTs into a macro-scale CNT material for bulk applications remains an unsolved challenge, with even the strongest materials only able to capture one-hundredth of the available individual CNT tensile strength [4,5]. To achieve resistivities of even 1.5×10^{-5} Ω cm requires several post-treatment steps, involving strong acids and iodine doping [6].

There are a number of different techniques to assemble individual CNTs into macro material products, such as spinning CNT fibers from a liquid-crystal phase, spinning fibers or pulling a continuous film from forest-grown CNTs [7,8]. However, spinning a film or fiber from a floating catalyst chemical vapor deposition (FCCVD) method is the most attractive as an industrially scalable route, by virtue of it being a one-step, continuous, gas-phase process and has already been adopted by several companies looking to exploit these advantages. The process, first described in detail by Li et al involves the continuous, controlled injection of a hydrocarbon source, an iron source (typically ferrocene vapor) and a sulfur source into a tubular reactor at temperatures above 1000°C in a reducing atmosphere (H_2 background) [9].

* Corresponding author. Tel: 01223 332600. E-mail: a.boies@eng.cam.ac.uk

Thermal decomposition of the iron and sulfur source leads to the nucleation of catalyst nanoparticles which act as a catalytic surface for CNT growth once sufficient carbon is available from the decomposition of the reactants. The role of sulfur is still under investigation but current research suggests it conditions the iron nanoparticles by affecting the carbon diffusivity at the surface and stimulating CNT growth [10,11]. As CNTs begin to grow, they preferentially bundle due to Van der Waals forces and these bundles intertwine to form an aerogel. The aerogel is mechanically drawn from the reactor tube onto a winding mechanism for continuous collection.

Understanding the impact of parameters such as the choice of carbon and catalyst precursors, the nature and ratio of sulfur-containing compounds to other reactants and the reaction temperature on CVD grown CNTs is increasingly well-documented [12]. However, extrapolating this information to the more complex continuous spinning of bulk CNT products from FCCVD processes is not straightforward. Parametric studies on how the morphology of bulk CNT products are affected by variables such as the carbon source, sulfur source and bulk flow rates indicate that while these factors do give some control, it is their interaction with the catalyst nanoparticles which is key to product purity [13–15]. The synthesis of undesired carbon structures for instance is reported to be influenced by secondary parameters including all of the above factors, with the control of sulfur being crucial [16]. Control of the formation of the iron-based catalyst nanoparticles is widely recognized as a primary parameter in controlling the diameter, purity, yield, crystalline quality, entanglements, chirality and number of walls of the CNTs in the final product and hence is an important factor in optimizing the bulk material properties [11,17]. The diameter of the catalyst nanoparticles closely correlates with the diameter of the CNTs, however it has recently been shown that in some CVD systems only 1% of iron based nanoparticles lead to CNT growth [18]. Some of the additional iron contributes to the co-synthesis of undesirable impurities such as graphitically-encapsulated nanoparticles, defective nanotubes and large diameter carbon tubules. These impurities are enmeshed in the CNT aerogel and disrupt the mechanical and electrical properties of the final product.

While some real-time analytical techniques such as TEM, XPS and Raman have been used to study the CVD growth of CNTs on substrates, studies of the relationship between catalyst nanoparticle formation and the synthesis of CNTs and impurities in FCCVD systems have principally relied on ex-situ post-experimental characterization [19–21]. An exception to this is the use of aerosol measurement techniques applied to both control catalytic nanoparticle size distributions prior to injection into a CVD system and to measure the synthesized CNTs at the exit [22–24].

In order to maximize the uptake of catalytic nanoparticles for CNT growth, and minimize or prevent the formation of unwanted side products, a much clearer understanding of the in-situ nanoparticle formation process is crucial for the industrial development of this FCCVD method. In the process, the catalyst nanoparticles initially nucleate from a vapor phase, which is created as the iron precursor (ferrocene) and sulfur precursor (thiophene) decompose. Besides nucleation, coagulation, surface growth, thermophoresis and diffusion affect nanoparticle growth. An experimentally-based analysis of the catalytic nanoparticle formation in real time along the axis of a tubular furnace will provide information on how these nanoparticles grow and where in the reactor bulk CNT material is generated. The present study investigates the production of catalyst nanoparticles within a CNT reactor in real time using a sampling system, which allows extraction and size distribution analysis of the catalyst particles from the hot reactor at multiple axial locations. Coupling the particle size distributions with velocity and thermal profiles, together with FTIR analysis of decomposition species synthesized from reactant inputs, provides new insight into the catalyst nanoparticle formation factors which influence both CNT and impurity formation.

2. Experimental Methods

The in situ experiments described in this paper were carried out in a horizontal tube furnace at ambient conditions and variable furnace temperatures. A schematic of the setup is shown in Fig. 1. Ferrocene (Acros, purity 98%) (~0.5 mass%) and Thiophene (Sigma Aldrich, purity ≥99%) (~3 mass%) as precursors diluted in a hydrogen (purity grade hydrogen N5.0, BOC) bulk flow of usually 0.5 slpm entered the reactor tube (40 mm ID and 700 mm length) through a showerhead injector which ensured a uniform and laminar inflow with a typical Reynold's number *Re*~25 (<<2300) at the inlet. All flow rates were controlled by mass flow controllers (Alicat). The injector face was placed ~50 mm from the inlet of the furnace tube such that the reactants entered the reactor space at approximately 200°C (compare Fig. 2). In-situ particle measurements were conducted by means of a TSI-Scanning Mobility Particle Sizer 3080 (SMPS) system including a TSI-Ultrafine Condensation Particle Counter 3776 (UCPC) and TSI-Differential Mobility Analyzers 3081 and 3085 (DMA) in an alumina (basis 99% Al_2O_3) furnace tube. Samples along the centerline were taken through a 1.9 mm ID alumina probe at flow rates inside the probe of 0.30 – 0.45 slpm and with help of an ejector system including a 0.04 mm (16/1000 inch) orifice. Typically a 1:50 dilution with pure and filtered ambient temperature nitrogen at the end of the probe was implemented. The data presented is corrected for dilution, diffusion and thermophoretic losses in the probe. Exhaust gases were vented to atmospheric pressure through a low pressure drop HEPA filter. An FT-IR spectrometer (Perkin Elmer Spectrum 100) fitted with a 10 cm path length gas cell was used to analyze gases at the exhaust.

In a further configuration methane (CH_4) was introduced at 0.06 slpm (N2.5, BOC) to the system, which served as a carbon source for CNT growth. Optical access was gained to the process by using a quartz furnace tube at 1200°C and performing a rapid shut down of all reactant gases while allowing the experiment to cool down in an argon (Ar) atmosphere (Ar purity N4.8, BOC). The morphology of the CNT aerogel that formed has then been investigated by means of scanning electron microscopy (Leo variable pressure SEM). Thermogravimetric analysis of the CNT product was carried out using a Mettler-Toledo TGA1 STAR^e system.

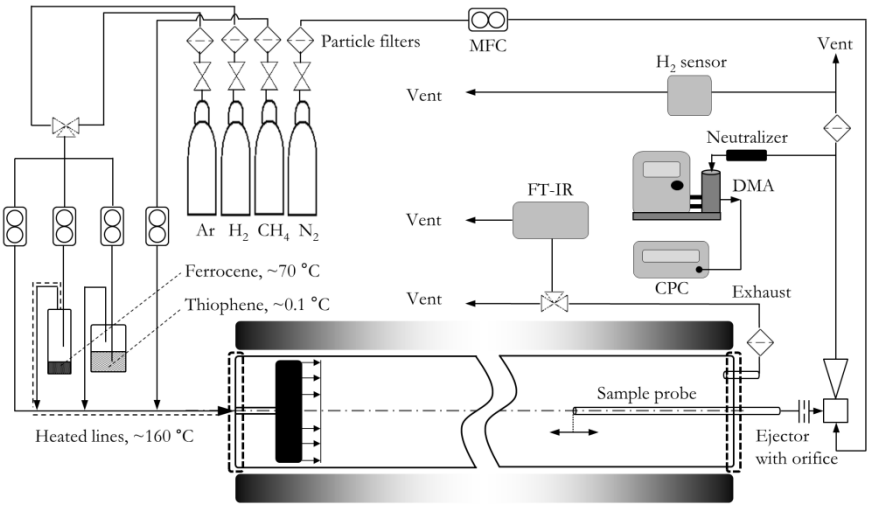

Fig. 1 - Schematic of the experimental setup using an injector to achieve a uniform inflow and a sample probe to measure in-situ catalyst particle size distributions.

3. Results and Discussion

3.1. *Flow and Temperature Profile in the Reactor*

The flow and temperature profile within the reactor (40 mm ID and 700 mm length) affect reactant decomposition, as well as nanoparticle nucleation, diffusion and thermophoretic phenomena. As shown in Fig. 2, the temperature difference between wall and centerline is small ($\Delta \boldsymbol{T_{max}}$~98°C) relative to the axial gradients, and the radial gradient changes from negative to positive down the centerline of the reactor. After injecting the reactants through a uniform flow injector reaching 50 mm into the reactor, it takes ~70 mm (1.75 equivalent diameters) for a fully-developed temperature and flow profile. The end of the reactor is closed and has a 4 mm wide exhaust which has a minor effect on the flow profile.

The temperature profile of the reactor is not constant and end-effects lead to a parabola shaped profile. The gas velocity inside the reactor and along its axis varies according to the ideal gas law, resulting in a centerline velocity that increases with increasing temperature. Conservation of mass, momentum and energy are taken into account in a 2D axisymmetric model of the reactor including set inlet and outlet conditions. Since the concentrations of ferrocene and thiophene in the hydrogen bulk flow are very low (< 0.06 vol%), chemical reactions and fluid properties of the minor species can be ignored and their dynamics are decoupled from fluid dynamics. A uniform inflow, axial wall temperature profile and atmospheric pressure are known for the experimental conditions, and are inputs to the CFD simulation. Because no gas slip occurs at the reactor wall, the gradient of velocity increases along the furnace, resulting in greater shear within the flow. Gravity and the contribution of CNTs to viscous forces are omitted but may play an important role in the velocity profile. No radiative heat transfer between CNTs and the tube wall is taken into account. The thermal diffusivity of energy from the walls into the reactor is proportional to the radial temperature gradient which is illustrated in Fig. 2 at different locations within the reactor tube. The radial gradient in temperature at the centerline is positive ($\mathbf{d}\boldsymbol{T}/\mathbf{d}\boldsymbol{r}_{\boldsymbol{r=0}}$>0) until $\boldsymbol{x}$≈360 mm and becomes negative for $\boldsymbol{x}$>360 mm. Unlike the velocity gradient, the gradient in temperature is at a minimum near the hottest region of the furnace and at a maximum near the entry and exit of the furnace. Given the temperature gradients between wall and centerline, the thermophoretic forces are driving particles away from the wall when $\mathbf{d}\boldsymbol{T}/\mathbf{d}\boldsymbol{r}$>0 for $\boldsymbol{x}$<360 mm and towards the wall when $\mathbf{d}\boldsymbol{T}/\mathbf{d}\boldsymbol{r}$<0 for $\boldsymbol{x}$>360 mm. The resulting drift velocity (V_{th}) of a catalyst nanoparticle (based on $\boldsymbol{V_{th}} = \frac{-0.55\boldsymbol{\mu}\boldsymbol{\nabla T}}{\boldsymbol{\rho_g T}}$, where $\boldsymbol{\mu}$ is the gas viscosity, $\boldsymbol{\nabla T}$ is the temperature gradient, $\boldsymbol{\rho_g}$ is the gas density and $\boldsymbol{T}$ is the absolute temperature of the particle, for particle diameters $\boldsymbol{d} < \boldsymbol{\lambda}$, where $\boldsymbol{\lambda}$ is the gas mean free path) upstream (180 mm<$\boldsymbol{x}$<240 mm) and downstream (540 mm<$\boldsymbol{x}$<600 mm) of the hottest point in the reactor is ~0.002 m/s (<8% of the centerline velocity) away from or towards the wall respectively [25].

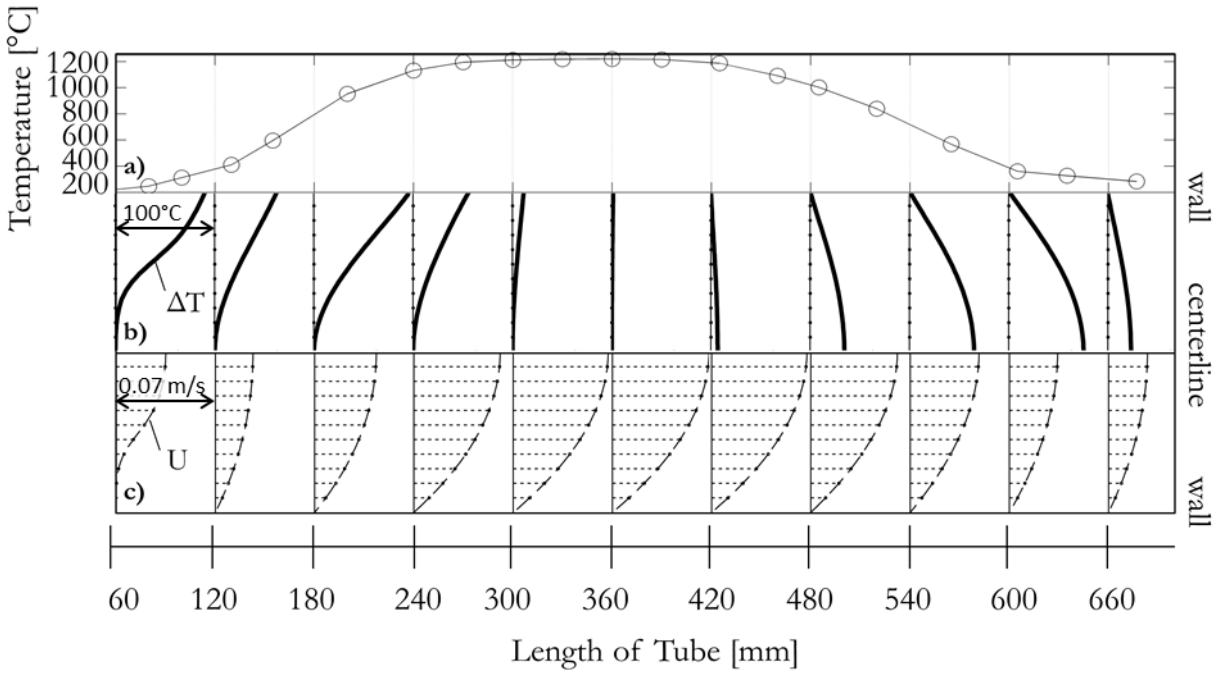

Fig. 2 - Flow and temperature profiles along the reactor axis, both measured and simulated for a hydrogen bulk flow of 0.5 slpm, a furnace set point of 1200°C and a radially uniform inflow into the reactor 50 mm from the reactor entrance; a) measured wall temperature in the reactor, b) modelled temperature gradients between wall and centerline with ΔT_{max} ~ 98°C, c) simulated velocity profiles in the reactor with U_{max} ~ 0.068 m/s.

3.2. *Decomposition of Ferrocene and Thiophene*

Studies of reactor chemistry via FT-IR spectroscopy offer insight into the decomposition profile of the reactants as the temperature changes throughout the reactor. The decomposition profile of ferrocene ($(C_5H_5)_2Fe$) and thiophene (C_4H_4S) within a H_2 environment is critical to the CNT growth mechanism, since they supply the precursor elements (Fe and S respectively) for the formation of the catalyst nanoparticles. The IR spectra measured at the reactor exit for thiophene alone at a variety of furnace set point temperatures are presented in Fig. 3a. The strong peak centred at ~710 cm^{-1} is characteristic of the out-of-plane wagging motion (ω_{oop}) of the C-H bond within the thiophene molecule, and is henceforth used as a reference marker to indicate its presence [26]. Increasing the furnace temperature to 750°C causes a decrease in intensity of the key thiophene band; this is also accompanied by the early onset of a doublet, an alkyne C triple bond stretch at ~2150 cm^{-1} (triple bond stretches are in the range of 2100-2180 cm^{-1}) [27]. The combination of the reduction in intensity of the thiophene marker, coupled with this doublet formation is indicative of the occurrence of a preliminary stage of pyrolysis, where triple-bonded carbon species are a common occurrence. Increasing the furnace temperature leads to further reduction in the thiophene peak, and the assigned alkyne resonance becomes more pronounced. Two further bands, associated with the presence of methane (decomposition product) are observed at 3020 cm^{-1} (anti-symmetric stretch (υ_{as})) and 1300 cm^{-1} (asymmetric bending mode (δ_{as})) respectively. By 1050°C, the thiophene marker is absent from the resultant IR spectrum indicating full decomposition.

Ferrocene spontaneously decomposes at temperatures higher than 500°C [28]. However, the rate of decomposition in a hydrogen environment is likely to be significantly reduced compared to that in a pyrolysis experiment. The impact of H_2 on the kinetics occurs because, in contrast to nickelocene and cobaltocene which decompose via the cleavage of the

metal-cyclopentadienyl bond, the first step in ferrocene decomposition is the breaking of a C-H bond. This leads to hydrogen gas as a pyrolysis product rather than 5-member carbon ring species [29]. As hydrogen is already present in the reactor in high concentration, the rate of ferrocene decomposition will be suppressed, leading to lower catalyst nanoparticle availability than might otherwise be anticipated, until the temperature rises further.

Whilst passing ferrocene through the reactor, IR spectra recorded within the temperature window of 450 - 750°C did not reveal any peaks characteristic to ferrocene (Fig. 3b), which is unsurprising as the sample lines between the reactor and the IR gas cell were unheated, so any ferrocene in the gas stream would condense onto the cool surfaces. However, resonance bands similar to those found in the analysis of thiophene, can be attributed to hydrocarbon-based decomposition products of ferrocene. These results demonstrate that ferrocene begins to decompose and form alkyne species at temperatures higher than 650°C in a hydrogen atmosphere at atmospheric pressure, correlating well with the proposed influence of H_2 on the kinetics of decomposition. Beyond the temperature of 750°C no increase in the concentration of decomposition products is observed, inferring that the decomposition is complete.

To determine whether the co-decomposition of ferrocene and thiophene occurs synergistically, a mixture of thiophene and ferrocene, at ratios typically used in the FCCVD process, was investigated revealing that the spectra resemble a superposition of the individual spectra obtained for thiophene and ferrocene alone. The decay of the thiophene marker in the presence and absence of ferrocene is illustrated in Figs. 3c-d, where the fact that the decay curves are nearly identical, suggests that the decomposition pathways for thiophene and ferrocene are independent from one another under the reaction conditions imposed.

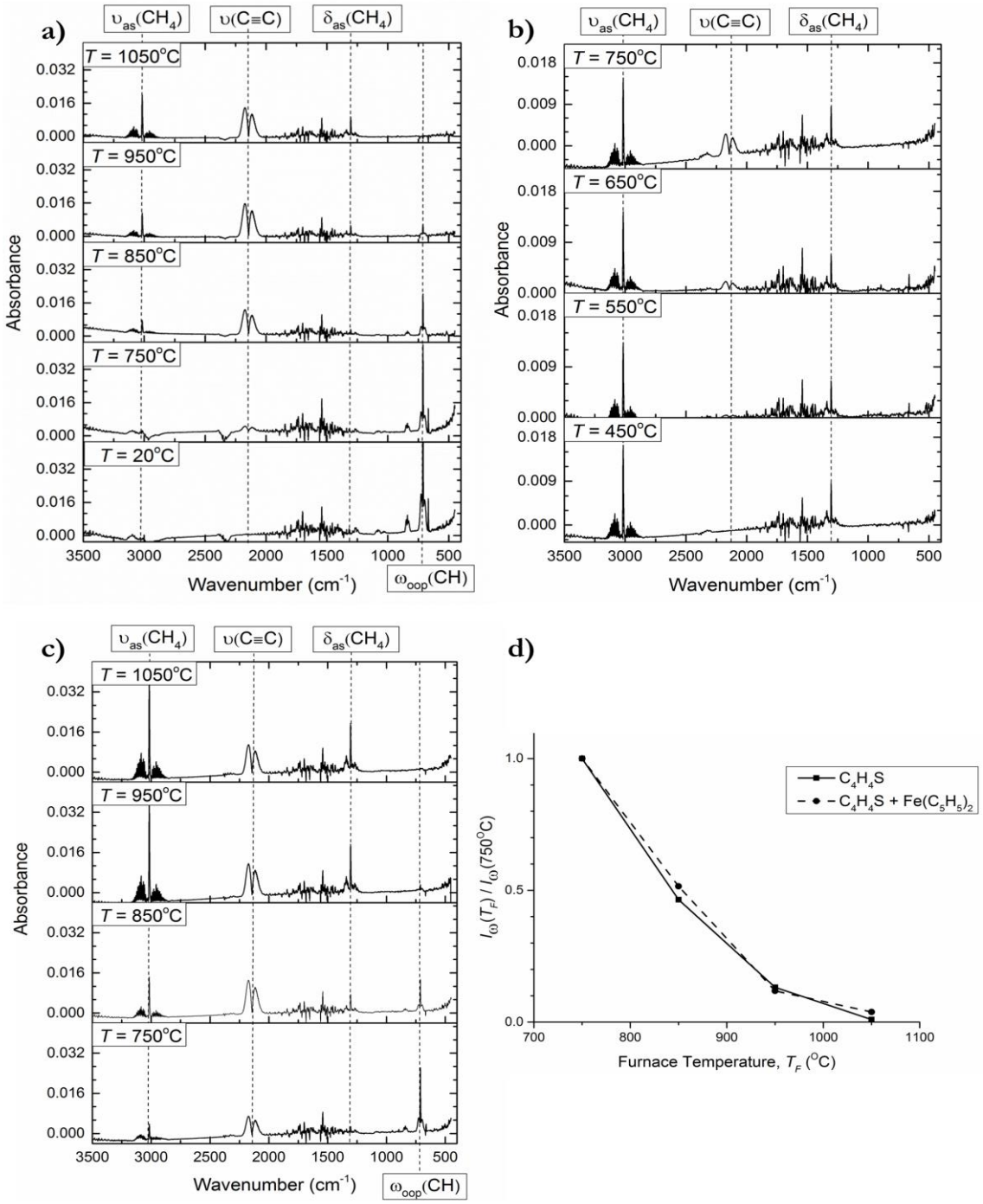

Fig. 3. - IR spectra taken from the exhaust of the reactor while decomposing a) thiophene, b) ferrocene and c) thiophene and ferrocene with varying reactor temperature settings with a reactor residence time of ~15 – 40 s depending on the temperature setting. d) Ratios of the intensity corresponding to the ω_{oop} mode of thiophene at a furnace temperature T_F ($I_\omega(T_F)$) relative to that measured at 750°C (I_ω(750°C)), for both thiophene alone and thiophene in the presence of ferrocene. The similarity of the intensities indicates the independence of the thiophene and ferrocene decomposition pathways.

3.3. *Particle Size Distributions along Reactor Axis*

In-situ axial measurements of catalyst nanoparticle size distributions along the centerline are analyzed to discern particle dynamics within the reactor. The properties of a catalyst nanoparticle, especially its size and chemical composition, influence the nature of the CNT growing from it. In-situ particle size measurements conducted without an additional source of carbon (e.g. CH_4) are shown in Fig. 4. The particle concentration rises abruptly down the central axis of the 700 mm long reactor from almost no particles ($<10^4$ #/cm^{-3}) upstream of 180 mm to high particle concentrations ($>10^8$ #/cm^{-3}) at ~200 mm. The rapid rise in particle concentration corresponds to temperatures (800-1050°C) where ferrocene and thiophene decomposition occurs (see Fig. 3 and Supporting Information Fig. S1), indicating that precursor decomposition leads to catalyst particle nucleation. Close examination of the temperature and spatial data indicates that the majority of nanoparticles (peak concentration ~10^9 #/cm^{-3}) are detected at temperatures greater than 1050°C (200-250 mm), thus bulk nucleation and detection of nanoparticles occur only after thiophene decomposition. Measurements further downstream show an almost immediate disappearance of particles at ~1200°C.

The nucleated particles appear as ~4 nm in diameter, which is near the lower detection limit of the SMPS (~3 nm). It is likely that the sampling method and applied corrections do not retroactively correct for all losses of small particles. Particle concentration increases and diameter grows as the aerosol moves from 200 mm to 300 mm. The peak of particle concentration is 7×10^8 #/cm^{-3} at ~1100°C for a furnace set point of 1150°C and ~10^9 #/cm^{-3} at ~1100°C for a furnace set point of 1300°C. Downstream of the measured peak particle concentration, the particle diameters decrease as the temperature increases, indicating particle-to-gas conversion (evaporation) as the saturation vapor pressure of iron rises with increased gas temperature down the furnace. This trend is strongly temperature dependent and leads to almost complete particle evaporation at a furnace set point of 1300°C. The iron based catalyst nanoparticles, which are presumably nano-droplets, have a higher vapor pressure compared to bulk material as described by the Gibbs-Thomson and Kelvin equations [30–32]. For lower furnace set points (1100-1200°C) particle size and concentration is reduced to a lesser extent, as the saturation vapor pressure of iron in the gas phase is lower. The maximum particle concentration occurs with a furnace temperature set point of 1300°C, the lowest is measured at a set point of 1150°C. Regardless of the furnace set points, the highest temperature-profile point within the furnace correspond to the lowest particle concentrations.

As the temperature drops at axial locations downstream of the maximum temperature (>450 mm), the particle concentration rises, indicating a second particle nucleation event. The second nucleation occurs as a result of a lower saturation vapor pressure of iron at lower furnace temperatures. Assuming that the bulk vapor pressure of iron is near the saturation vapor pressure at the maximum temperature within the furnace (maximum concentration of iron in the gas phase), the decrease in saturation vapor pressure as the reactor cools, leads to supersaturation of iron in the gas phase. The supersaturation results in particle nucleation, increasing the concentration of catalyst particles in the reactor. While particle concentration rises in the downstream section, the number of catalyst particles is not as high as for the initial nucleation event mainly due to presumed losses to the reactor walls.

The total mass of catalyst nanoparticles, based on the SMPS-measured particle size distribution, is shown in Fig. 6. Particle mass is a maximum just before the hottest zone and then drops as temperature increases, again indicating particle-to-gas conversion. As the temperature decreases in the downstream half of the furnace particle mass increases, consistent with particle number shown above. Total system particle mass is a maximum for a furnace set point of 1250°C, indicating that at higher furnace set point temperatures the rise in the iron saturation vapor pressure results in less particle-phase iron despite greater rates of precursor decomposition, and thus iron availability, at higher temperatures. At a set point temperature of 1300°C no mass is detectible from 400 to 500 mm, indicating complete

particle evaporation. For lower furnace set points (1100-1200°C) particle-phase catalysts remain throughout the reactor with a minimum total system particle mass of ~500 μg/m^3 throughout the highest temperature region. Diffusion and thermophoretic losses cannot account for the rapid change in particle mass and concentration between 250 – 400 mm as a penetration of minimum 30 – 90%, depending on the particle diameter, can be expected (Supporting Information Fig. S2). This indicates that particle evaporation is likely the dominant loss mechanism. As the temperature decreases downstream of the maximum temperature, the re-nucleation of catalyst nanoparticles results in an increase in particle mass concentration. At lower furnace set points more mass is recovered but re-nucleated particles do not achieve the same total mass as the upstream concentration. Loss of particle mass is a result of the nucleation of iron on the downstream reactor wall, as well as diffusion of catalyst nanoparticles to the wall. Also sulfur, which may amount to up to half of the total solid mass measured upstream of the hottest zone, will likely remain in the gas phase as H_2S once the temperature is dropping downstream the hottest zone.

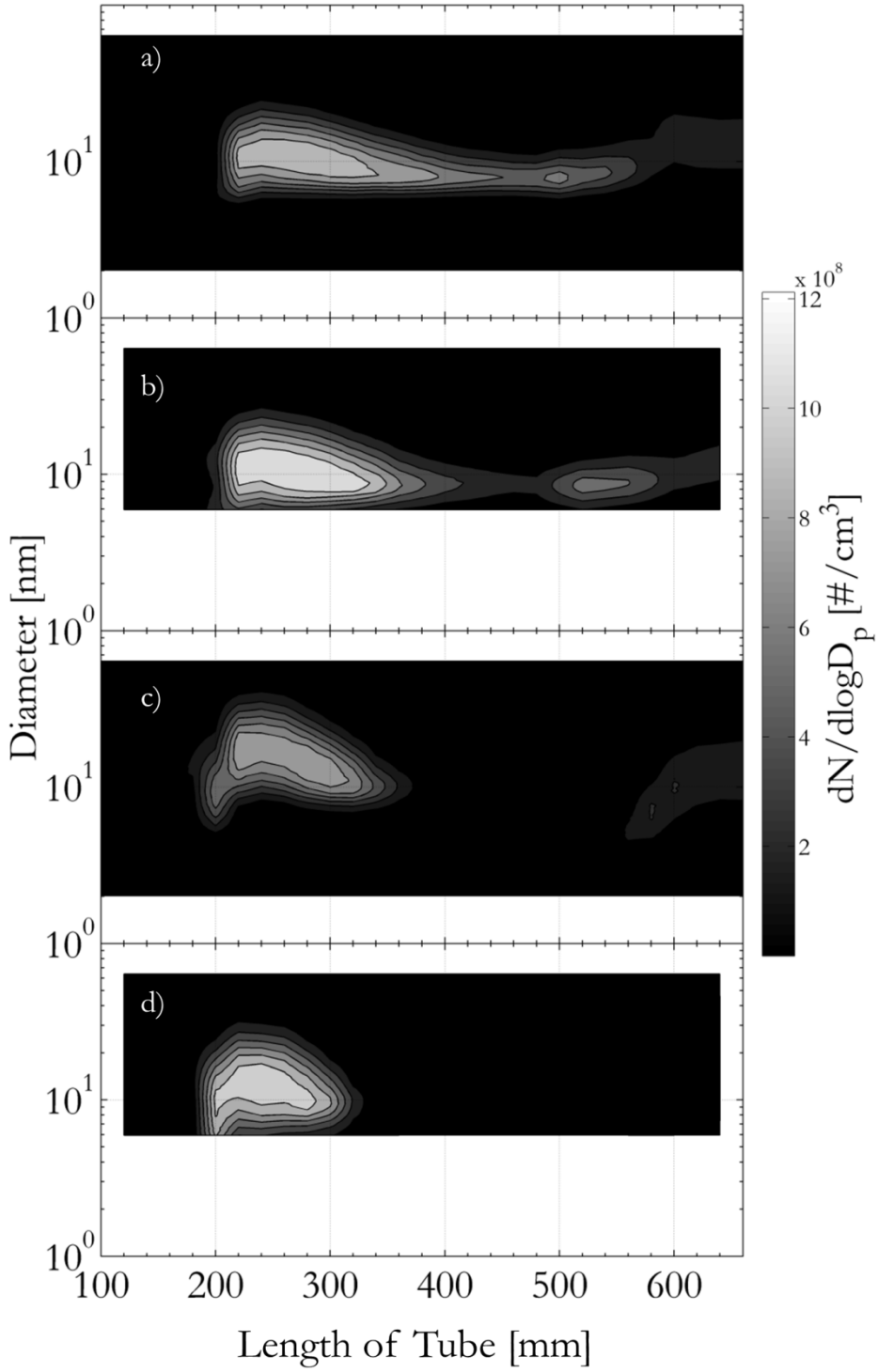

Fig. 4 - In-situ measurements of catalyst particle size distributions along the reactor axis for different furnace temperature set-points and at a bulk hydrogen flowrate of 0.5 slpm; a) 1150°C, b) 1200°C, c) 1250°C, d) 1300°C.

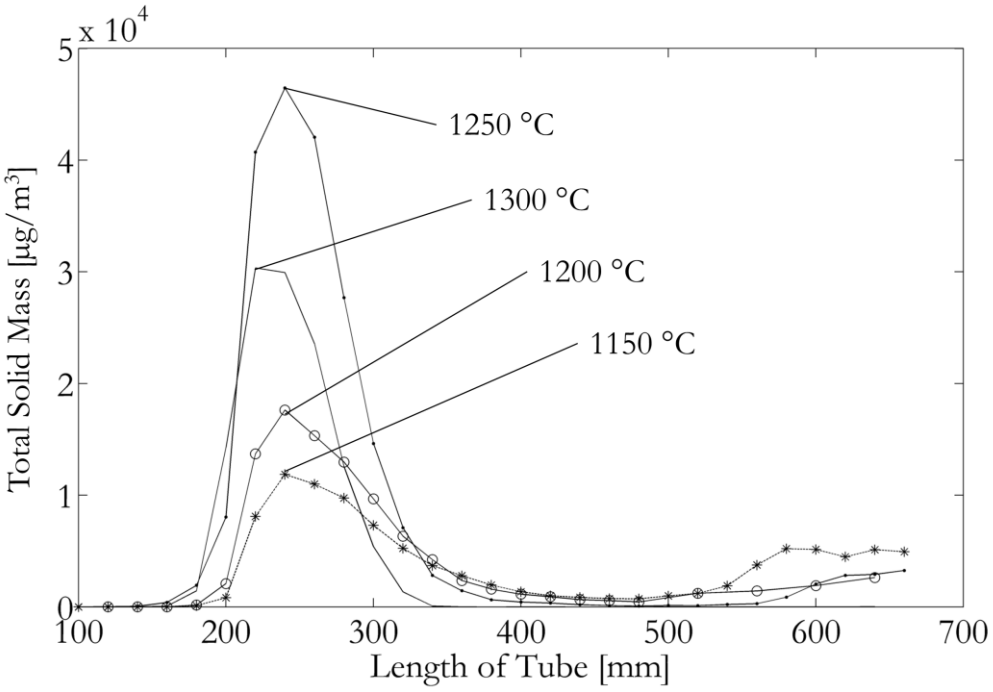

Fig. 5 - Total solid mass in the form catalyst nanoparticles along the reactor axis for different furnace temperature set points measured at a hydrogen bulk flowrate of 0.5 slpm.

3.4. *CNT Formation and Fiber Morphology*

In studies with CH_4 being present as a carbon source, samples of CNT materials were collected along the tube axis after stopping the reactants and allowing the reactor to cool in an Ar atmosphere. TGA analysis of bulk material collected at the reactor exit reveals an iron content by mass of ~11%. Amorphous carbon accounts for ~10% of the carbon based species in the CNT product whereas ~90% is CNT-based, which is in the typical range of other FCCVD CNT fiber material [18,33]. SEM (Fig. 6) and optical (Fig. 7c) images from the Ar-cooled tube reveal different nano and macro morphologies of CNT materials along the axis of the reactor. Visual examination of the reactor tube shows that a continuous macroscopic fiber consisting of CNTs begins at ~170 mm from the reactor entrance and extends to the tube exit, with a significant increase in the concentration of CNT aerogel-growth in the final section of the reactor.

The start of the fiber is attached to the reactor wall at the location in the reactor zone where thiophene decomposition begins and the rate of ferrocene decomposition is increasing rapidly at a temperature of ~700 °C, identified by the thermal decomposition FTIR studies reported in section 3.2 and backed up by the carbon deposition bands shown in Fig. 7c and comparison photographs in Fig. S1.. At this early location CNT bundles (diameters 15–35 nm) and individual CNTs, mainly oriented along the gas flow, can be found (Figs. 6d). Only a very small number of catalyst nanoparticles are attached to these small CNT-bundles, correlating well with the low nanoparticle concentration and total solid mass shown in Figs. 7a-b. Based on the FTIR evidence, the carbon for CNT formation in this zone must come principally from either the thermal decomposition of ferrocene or thiophene or catalytic decomposition of CH_4 on the forming catalyst nanoparticles.

As the temperature increases along the reactor axis, both ferrocene and thiophene break down increasingly rapidly and the initially-grown CNTs act as a surface for heterogeneous nucleation of catalytic nanoparticles (Figs. 6c). CNT growth occurs in parallel with nanoparticle nucleation and bundling of CNTs due to Van der Waals forces as well as branching of the bundles can be observed.

The CNTs further down the tube axis (~>330 mm) are essentially free of attached catalyst nanoparticles (Figs. 6b). The nanoparticles disappear as the temperature increases towards 1200°C, further reinforcing the evidence of particle evaporation presented in section 3.3. Any remaining nanoparticles attached to the earlier-grown CNTs potentially catalyze further CNT growth through this zone of the reactor, continuing to use any remaining carbon from ferrocene and thiophene decomposition and additionally CH_4, as the temperatures are sufficient to cause catalytic and thermal decomposition.

Downstream of the maximum temperature zone, as the temperature drops (~>420 mm), catalyst nanoparticle re-nucleation occurs from the iron-rich vapour causing the growth of more CNTs but also of carbonaceous impurities such as encapsulated iron nanoparticles and large diameter deformed and clustered CNTs which become embedded in the CNT aerogel (Figs. 6a). The carbon for this growth is supplied in abundance from the decomposition of CH_4 in the high-temperature region of the reactor where there were few, if any, catalyst nanoparticles available for it to immediately react with. This observation regarding the main location of impurity formation contrasts with publications such as [16] which hypothesises that the growth of large, defective carbonaceous species in CH_4-based FCCVD processes begins at the same time as narrow-diameter CNTs form.

To further confirm where the bulk CNT growth occurs along the reactor profile, electrical resistance measurements between reactor wall and the outlet were carried out after the fiber reaching through the furnace tube was taken out. Starting near the hottest zone (>320 mm), the tube wall becomes increasingly electrically conductive ($\boldsymbol{R}<10^6\ \Omega$) indicating a CNT coating at the wall (Fig. 7d). Microscopy analysis of material collected from the wall confirms these results (Supporting Information Fig. S3).

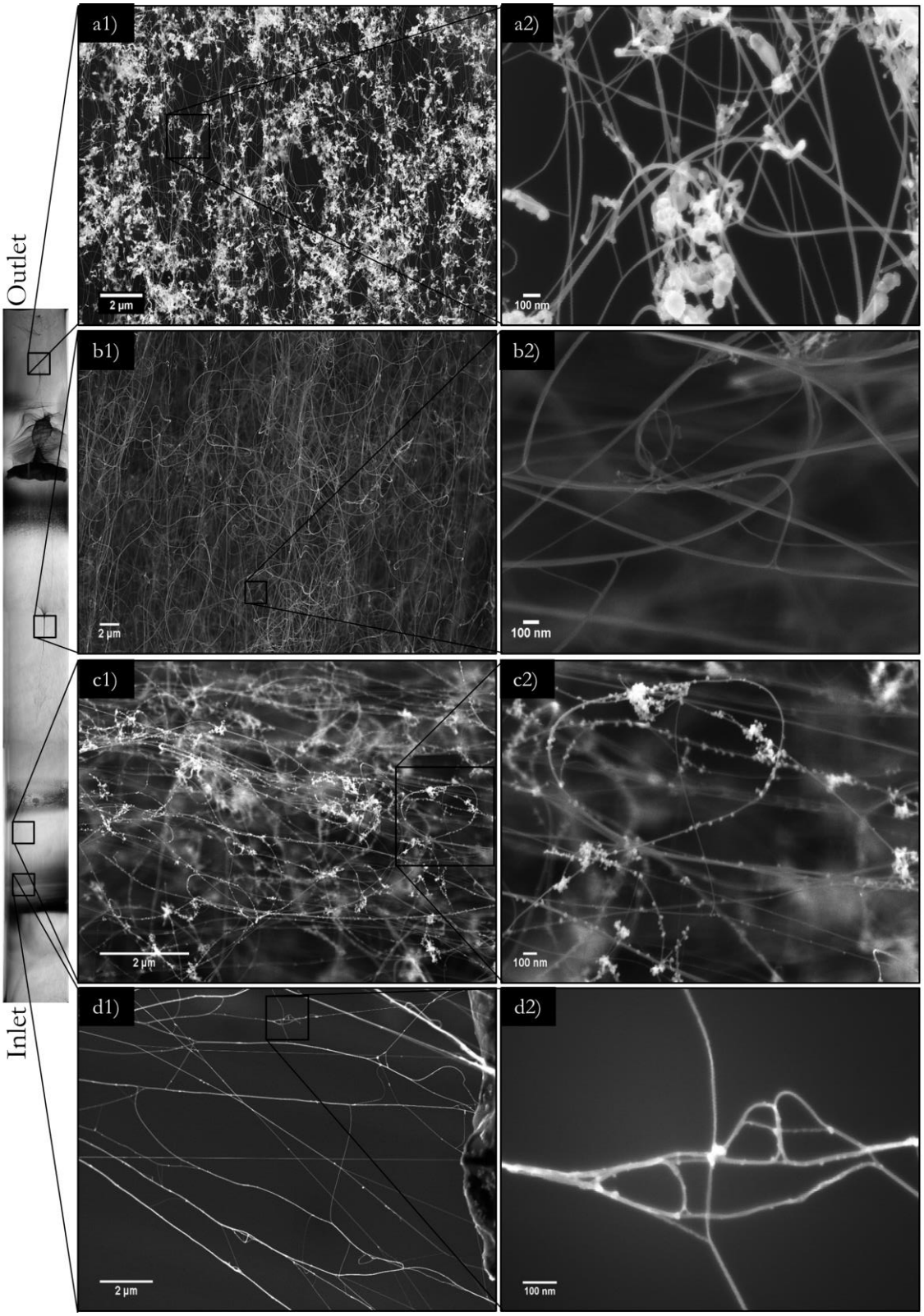

Fig. 6 - SEM images of CNTs formed in the reactor at different axial locations. The nature of the impurities and their concentration in the CNT material change depending on the location and the corresponding temperature with a) being closest to the outlet and d) nearest to the inlet.

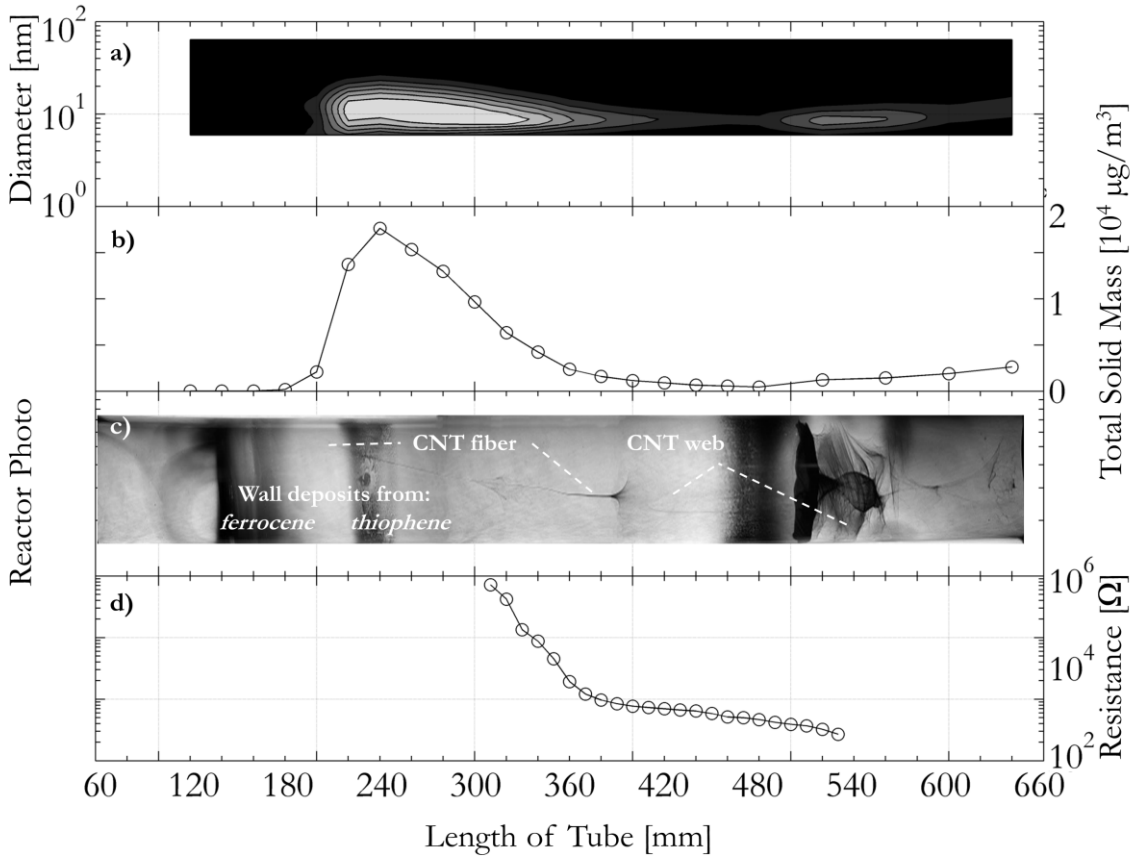

Fig. 7 - Overview of different measurements along the reactor at a set point of 1200°C and a hydrogen bulk flowrate of 0.5 slpm; a) centerline particle size distribution, b) total solid mass measured, c) reactor photo showing different macro morphologies of CNT fiber and aerogel and indicating the decomposition regions of the reactants, d) resistance between reactor wall and exit flange, measured after removal of the aerogel material.

4. Conclusion

Infrared spectrometry results demonstrate that the catalyst particle precursors (ferrocene and thiophene) decompose independently from one another within narrow temperature dependent zones, indicating that the *onset* of the decomposition of each species is primarily thermally rather than catalytically driven.

Catalyst nanoparticles nucleate and grow as a result of the precursor decomposition. Size distribution measurements along the reactor axis show a distinctive, temperature dependent variation in catalyst nanoparticle concentration and size due to temperature-dependent changes in the saturation vapor pressure of iron throughout the reactor. The dynamics of the catalyst nanoparticles (e.g. nucleation, condensation and evaporation) impacts the growth and concentration levels of impurities found in the resulting CNT material. The work presented herein corresponds to findings of larger CNT pilot-scale reactors with similar (approximately the same diameter to length ratio and system velocities). Thus, these results may generally be applied to reactors of different size as long as the flow is fully developed, the reactant concentrations are comparable and the furnace has a similar temperature profile i.e. parabolic. Within our laboratory reactor the phenomena described

above were observed for all reactor conditions that could produce viable CNT material, and are thus thought to be general.

Four specific regions of CNT aerogel production have been shown by SEM analysis to consist of different structural features that directly correlate to the nanoparticle behavior. At the beginning of the reaction zone, homogeneous nanoparticle nucleation in a carbon-lean environment stimulates the growth of CNT material with a low impurity profile. This is followed by a region characterized by a higher impurity concentration where both heterogeneous nucleation of individual catalyst particles on the existing CNT structures and agglomeration of nanoparticles contribute. Graphitic encapsulation of some of these paricles is also likely to occur. The hottest zone of the reactor exhibits the lowest impurity profile due to the evaporation of non-encapsulated nanoparticles, leaving an essentially clean CNT material and substantial CNT formation and growth will taking place in parallel. Towards the reactor exit, the decrease in temperature results in re-nucleation of iron-based nanoparticles from a saturated vapor in a carbon rich environment, which leads to a burst in the growth of carbon nanostructures, including a high concentration of carbon-based impurities.

This work highlights the extent to which precursors, nanoparticles and CNTs are influenced by the spatial and temperature variations within a floating catalyst CNT reactor. Our results also indicate that the level of impurities could be controlled by reactor design modifications which may drastically improve the resulting CNT product.

Acknowledgements
The authors thank Qflo Ltd for providing funding towards this research, C. Hoecker additionally thanks Churchill College Cambridge for financial support, M. Bajada gratefully acknowledges financial support through the 'Master it! Scholarship Scheme'. C. Hoecker and F. Smail contributed equally to this work.

[1] Wang M-S, Golberg D, Bando Y. Tensile tests on individual single-walled carbon nanotubes: linking nanotube strength with its defects. Adv Mater 2010;22:4071–5. doi:10.1002/adma.201001463.

[2] Kim P, Shi L, Majumdar A, McEuen P. Thermal Transport Measurements of Individual Multiwalled Nanotubes. Phys Rev Lett 2001;87:215502. doi:10.1103/PhysRevLett.87.215502.

[3] Schönenberger C, Bachtold A, Strunk C, Salvetat JP, Forró L. Interference and interaction in multi-wall carbon nanotubes. Appl Phys A Mater Sci Process 1999;69:283–95. doi:10.1007/s003390051003.

[4] Zhang X, Li Q, Tu Y, Li Y, Coulter JY, Zheng L, et al. Strong carbon-nanotube fibers spun from long carbon-nanotube arrays. Small 2007;3:244–8. doi:10.1002/smll.200600368.

[5] De Volder MFL, Tawfick SH, Baughman RH, Hart AJ. Carbon Nanotubes: present and Future Commercial applications. Science 2013;339:535–9. doi:10.1126/science.1222453.

[6] Zhao Y, Wei J, Vajtai R, Ajayan PM, Barrera E V. Iodine doped carbon nanotube cables exceeding specific electrical conductivity of metals. Sci Rep 2011;1:83. doi:10.1038/srep00083.

[7] Behabtu N, Young CC, Tsentalovich DE, Kleinerman O, Wang X, Ma AWK, et al. Strong, light, multifunctional fibers of carbon nanotubes with ultrahigh conductivity. Science 2013;339:182–6. doi:10.1126/science.1228061.

[8] Huynh CP, Hawkins SC. Understanding the synthesis of directly spinnable carbon nanotube forests. Carbon 2010;48:1105–15. doi:10.1016/j.carbon.2009.11.032.

[9] Li Y-L, Kinloch IA, Windle AH. Direct spinning of carbon nanotube fibers from chemical vapor deposition synthesis. Science 2004;304:276–8. doi:10.1126/science.1094982.

[10] Motta MS, Moisala A, Kinloch IA, Windle AH. The role of sulphur in the synthesis of carbon nanotubes by chemical vapour deposition at high temperatures. J Nanosci Nanotechnol 2008;8:2442–9. doi:10.1166/jnn.2008.500.

[11] Yu F, Yang M, Li F, Su C, Ma B, Yuan Z, et al. The growth mechanism of single-walled carbon nanotubes with a controlled diameter. Phys E Low-Dimensional Syst Nanostructures 2012;44:2032–40. doi:10.1016/j.physe.2012.06.007.

[12] Jourdain V, Bichara C. Current understanding of the growth of carbon nanotubes in catalytic chemical vapour deposition. Carbon 2013;58:2–39. doi:10.1016/j.carbon.2013.02.046.

[13] Sundaram RM, Windle AH. Effect of Carbon Precursors on the Structure and Properties of Continuously Spun Carbon Nanotube Fibers. Sci Adv Mater 2015;7:643–53. doi:10.1166/sam.2015.2147.

[14] Sundaram RM, Koziol KKK, Windle AH. Continuous direct spinning of fibers of single-walled carbon nanotubes with metallic chirality. Adv Mater 2011;23:5064–8. doi:10.1002/adma.201102754.

[15] Motta M, Kinloch I, Moisala A, Premnath V, Pick M, Windle A. The parameter space for the direct spinning of fibres and films of carbon nanotubes. Phys E Low-Dimensional Syst Nanostructures 2007;37:40–3. doi:10.1016/j.physe.2006.07.005.

[16] Gspann T, Smail F, Windle A. Spinning of carbon nanotube fibres using the floating catalyst high temperature route: purity issues and the critical role of sulphur: Supporting Online Material 1. Faraday Discuss 2014;173:2–7. doi:10.1039/C4FD00066H.

[17] Nessim GD, Hart AJ, Kim JS, Acquaviva D, Oh J, Morgan CD, et al. Tuning of vertically-aligned carbon nanotube diameter and areal density through catalyst pre-treatment. Nano Lett 2008;8:3587–93. doi:10.1021/nl801437c.

[18] Reguero V, Alemán B, Mas B, Vilatela JJ. Controlling Carbon Nanotube Type in Macroscopic Fibers Synthesized by the Direct Spinning Process. Chem Mater 2014;26:3550–7.

[19] Ichihashi T, Fujita J, Ishida M, Ochiai Y. In situ Observation of Carbon-Nanopillar Tubulization Caused by Liquidlike Iron Particles. Phys Rev Lett 2004;92:215702. doi:10.1103/PhysRevLett.92.215702.

[20] Sehested J, Hansen PL, Helveg S, Lo C, Clausen BS, Rostrup-Nielsen JR, et al. Atomic-scale imaging of carbon nanofibre growth. Nature 2004;427:5–8. doi:10.1038/nature02308.1.

[21] Hofmann S, Sharma R, Ducati C, Du G, Mattevi C, Cepek C, et al. In situ observations of catalyst dynamics during surface-bound carbon nanotube nucleation. Nano Lett 2007;7:602–8. doi:10.1021/nl0624824.

[22] Kim SH, Zachariah MR. In-flight size classification of carbon nanotubes by gas phase electrophoresis. Nanotechnology 2005;16:2149–52. doi:10.1088/0957-4484/16/10/030.

[23] Moisala A, Nasibulin AG, Shandakov SD, Jiang H, Kauppinen EI. On-line detection of single-walled carbon nanotube formation during aerosol synthesis methods. Carbon 2005;43:2066–74. doi:10.1016/j.carbon.2005.03.012.

[24] Mustonen K, Susi T, Nasibulin AG, Jiang H, He M, Kauppinen EI. Direct synthesis of high-quality single-walled carbon nanotubes by the physical nucleation of iron nanoparticles in an atmospheric pressure carbon monoxide flow. Carbon 2012;50:5343–5. doi:10.1016/j.carbon.2012.07.006.

[25] Hinds WC. Aerosol Technology: Properties, Behaviour and Measurement of Airborne Particles, Second Edition. New York, USA: John Wiley & Sons, Inc; 1999.

[26] Mills P, Korlann S, Bussell ME, Reynolds MA, Ovchinnikov M V, Angelici RJ, et al. Vibrational Study of Organometallic Complexes with Thiophene Ligands : Models for Adsorbed Thiophene on Hydrodesulfurization Catalysts 2001:4418–29.

[27] Bruno T, Svoronos P. No Title. In: Haynes W, editor. CRC Handb. Chem. Phys. 96th ed., Taylor and Francis; 2015.

[28] Leonhardt a., Hampel S, Müller C, Mönch I, Koseva R, Ritschel M, et al. Synthesis, Properties, and Applications of Ferromagnetic-Filled Carbon Nanotubes. Chem Vap Depos 2006;12:380–7. doi:10.1002/cvde.200506441.

[29] Elihn K, Larsson K. A theoretical study of the thermal fragmentation of ferrocene. Thin Solid Films 2004;458:325–9. doi:10.1016/j.tsf.2003.12.058.

[30] Flagan R, Seinfeld J. Fundamentals of Air Pollution Engineering, New Jersey: Prentice-Hall, Inc; 1988, p. 290–396.

[31] Kaptay G. The Gibbs Equation versus the Kelvin and the Gibbs-Thomson Equations to Describe Nucleation and Equilibrium of Nano-Materials. J Nanosci Nanotechnol 2012;12:2625–33. doi:10.1166/jnn.2012.5774.

[32] Chakraborty AK, Jacobs J, Anderson C, Roberts CJ, Hunt MRC. Chemical vapor deposition growth of carbon nanotubes on Si substrates using Fe catalyst: What happens at the nanotube/Fe/Si interface. J Appl Phys 2006;100:084321. doi:10.1063/1.2360774.

[33] Zhong X-H, Li Y-L, Liu Y-K, Qiao X-H, Feng Y, Liang J, et al. Continuous multilayered carbon nanotube yarns. Adv Mater 2010;22:692–6. doi:10.1002/adma.200902943.